



**HAL**  
open science

## Magnetism in LAMOST CP stars observed by TESS

K. Thomson-Paressant, C. Neiner, J. Labadie-Bartz

► **To cite this version:**

K. Thomson-Paressant, C. Neiner, J. Labadie-Bartz. Magnetism in LAMOST CP stars observed by TESS. *Astronomy & Astrophysics - A&A*, 2024, 689, pp.A208. 10.1051/0004-6361/202450651 . hal-04697720

**HAL Id: hal-04697720**



**<https://hal.science/hal-04697720v1>**

Submitted on 14 Sep 2024

**HAL** is a multi-disciplinary open access archive for the deposit and dissemination of scientific research documents, whether they are published or not. The documents may come from teaching and research institutions in France or abroad, or from public or private research centers.

L'archive ouverte pluridisciplinaire **HAL**, est destinée au dépôt et à la diffusion de documents scientifiques de niveau recherche, publiés ou non, émanant des établissements d'enseignement et de recherche français ou étrangers, des laboratoires publics ou privés.

# Magnetism in LAMOST CP stars observed by TESS

K. Thomson-Paressant<sup>\*</sup> , C. Neiner , and J. Labadie-Bartz

LESIA, Paris Observatory, PSL University, CNRS, Sorbonne University, Université Paris Cité, 5 Place Jules Janssen, 92195 Meudon, France

Received 8 May 2024 / Accepted 19 June 2024

## ABSTRACT

**Context.** A thousand new magnetic candidate CP stars have been identified with LAMOST, of which  $\sim 700$  prime targets have had rotational modulation determined by TESS.

**Aims.** We aim to check for the presence of a magnetic field in a subsample of these LAMOST CP stars, test the viability of the 5200 Å depression used to select the mCP candidates in the LAMOST survey as a reliable indicator of magnetism, and expand on the limited database of known magnetic hot stars. The sample includes some pulsators that would be valuable targets for magneto-asteroseismology.

**Methods.** We selected  $\sim 100$  magnetic candidate LAMOST CP stars that present a depression at 5200 Å in their spectrum and that also display rotational modulation in their TESS photometric light curves. We obtained spectropolarimetric observations of 39 targets from this sample with ESPaDOnS at CFHT. We utilised the least squares deconvolution method to generate the mean profile of the Stokes  $V$  and  $I$  parameters, from which the longitudinal magnetic field strength for each target can be determined. For HD 49198, we performed more in-depth analysis to determine the polar magnetic field strength and configuration.

**Results.** We detect fields in at least 36 of the 39 targets in our sample. This success rate in detecting a magnetic field (above 92%) is very high compared to the occurrence of magnetic fields in hot stars ( $\sim 10\%$ ). Four of these newly discovered magnetic stars are magnetic pulsators. In particular, we detect the strongest field around a  $\delta$  Scuti star discovered to date: a 12 kG dipolar field in HD 49198.

**Conclusions.** From our analysis, we conclude that using the 5200 Å depression displayed in the spectra in combination with rotational modulation in photometric data is a very reliable method of identifying magnetic candidates in this population of stars.

**Key words.** stars: chemically peculiar – stars: magnetic field – stars: oscillations

## 1. Introduction

Chemically peculiar (CP) stars are typically main sequence stars that present atypical abundances of certain chemical elements in their surface layers. There are a number of different CP classes, depending on what features they display and what over- or under-abundances they display in their spectra (Ap/Bp, He-strong, He-weak, HgMn, Si, etc.; see Preston 1974). It is believed that these chemical peculiarities appear after the formation of the star, as part of its evolution, due to processes such as atomic diffusion or magnetic effects, which dredge chemical elements up to the surface layers or settle in the interior (Michaud 1970; Alecian 1986). The CP stars account for approximately 10% of main sequence intermediate-mass stars between early-F and early-B (Wolff 1968; Aurière et al. 2007; Kochukhov 2009; Sikora et al. 2019), and a further 10% of OBA main sequence stars present a strong, large-scale magnetic field (Donati & Landstreet 2009; Ferrario et al. 2015; Fossati et al. 2015). These two subsets have a significant overlap, corresponding to magnetic CP (mCP) stars with field strengths ranging from  $\sim 0.1$ –30 kG (Babcock 1960; Landstreet 1982), mainly of the Ap/Bp-type.

These mCP stars are key observation targets for several reasons. The mechanisms at the origin of their chemical peculiarity (i.e. atomic diffusion, magnetic fields, rotation, and combinations of these) are in and of themselves interesting phenomena to study to garner a better understanding of stellar physics and stellar evolution. In addition, their complex atmospheres are great

examples with which we can test and evaluate the validity of atmospheric models, and the variability in their light curves due to chemical spots allows for the precise determination of their rotation periods, a benefit that is essential for the study of stellar magnetism (Hümmerich et al. 2018).

Pulsating stars along the instability strips on the Hertzsprung-Russell (HR) diagram (e.g.  $\delta$  Scuti,  $\gamma$  Doradus,  $\beta$  Cephei, etc.) can also display chemical peculiarities and, since this is typically a good indicator of magnetism, these candidates are very appealing targets for magneto-asteroseismology. Pulsating stars allow us to probe their stellar interiors and physical processes; thus, they provide key insights into how stars in general form and evolve throughout the HR diagram (Kurtz 2022). Coupling this pulsational information with knowledge of the magnetic field structure for these stars puts strong constraints on seismic models.

Through the magnetic analysis of CP stars presented in this paper, we aim to expand the list of known mCP stars and prove the validity of using the 5200 Å depression to infer magnetism within this family of stars. This is particularly valuable for the subset of pulsating variable stars contained within this sample, as the number of confirmed magnetic pulsators is very limited. In addition, a detailed magnetic analysis is performed for one of the targets. In-depth analysis of these stars will allow for the constraining of magneto-asteroseismic models, which in turn will provide a better understanding of the influence magnetic fields have on the internal structure of stars and a way to probe the magnetic field inside the star.

\* Corresponding author; keegan.thomson-paressant@obspm.fr

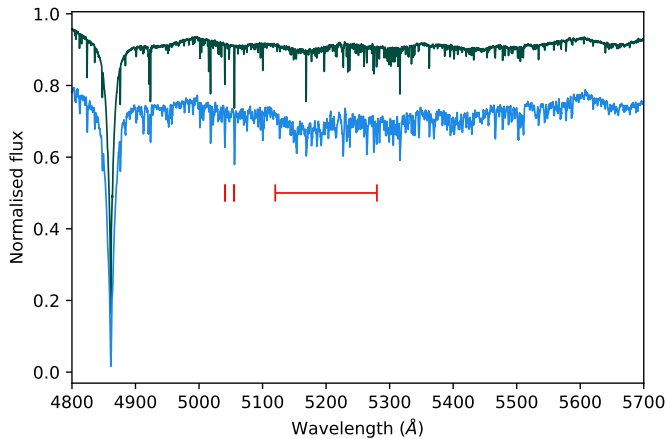


**Fig. 1.** Visualisation of the 5200 Å region (red bar) for non-CP star HD 220575 (top), and of confirmed mCP star HD 212714 (bottom). Both stars have a similar spectral type (B8) and their spectra were both taken with the ESPaDOnS instrument. The characteristic Si II lines at 5041 and 5055 Å are also indicated (red tick marks).

## 2. Target selection

The Large Sky Area Multi-Object Fibre Spectroscopic Telescope (LAMOST, Zhao et al. 2012; Cui et al. 2012), operating at the Xinglong Station in China, was designed to perform a spectroscopic survey of 10 million stars in the Milky Way, as well as millions in other galaxies. Since its first data release in June 2013, it has released additional datasets each year, and it has recently surpassed its scientific goals.

From the initial LAMOST survey, containing some 4 million stars, a sub-sample of 1002 candidate mCP stars was determined by Hümmelich et al. (2020). This was done by selecting all targets that contained a depression at 5200 Å in the LAMOST DR4 spectra of early-type stars (see Fig. 1). This depression at 5200 Å, along with ones at 1400, 1750, 2750, 4100, and 6300 Å, was determined to be uniquely characteristic of mCP stars (Maitzen 1976; Kupka et al. 2003, 2004; Khan & Shulyak 2007; Stigler et al. 2014). In particular, it was found that Fe is the primary contributor to the 5200 Å depression, and that the latter is present for the whole range of effective temperatures in mCP stars, making it a fantastic indicator of magnetism in these stars. All the stars in this subset are between 100 Myr and 1 Gyr old, with masses between 2–3  $M_{\odot}$ .

This subset was then cross-checked with photometry from the Transiting Exoplanet Survey Satellite (TESS, Ricker et al. 2015) to look for variability in their light curves, and determine stellar parameters such as the rotation period and pulsation frequencies (Labadie-Bartz et al. 2023). Through this analysis, Labadie-Bartz et al. (2023) determined the rotation periods for 720 mCP stars, including 25 showing signals consistent with pulsation.

From here, stars that had  $m_V \lesssim 10$ ,  $v \sin i \lesssim 100 \text{ km s}^{-1}$ , required <6 hours of observation time with CFHT/ESPaDOnS to achieve a theoretical magnetic field detection threshold of 300 G and displayed rotational modulation in their photometric light curves was maintained in the selection. From a list of ~100 targets, the sample presented here is in the end composed of 39 stars suitable for follow-up spectropolarimetric observations to look for magnetic fields (Buyschaert et al. 2018; Thomson-Paressant et al. 2023), with a particular emphasis on

those that were found to display pulsation signatures in the previous step.

## 3. Spectropolarimetric observations

The targets in our sample were observed with the Echelle SpectroPolarimetric Device for the Observation of Stars (ESPaDOnS, Donati et al. 2006), operating on the Canada France Hawaii Telescope (CFHT) at Mauna Kea Observatory in Hawaii. The observations primarily took place over four semesters between February 23, 2021 and July 18, 2022, but with a few additional observations being performed during January 2024. The list of targets and their respective observations are available in Table A.1. The exposure time used for each target was defined by considering the stellar properties (in particular temperature and  $v \sin i$ ) and assuming that the field possibly present in the targets is at least 300 G. Studies suggest that magnetic OBA stars typically have a magnetic field strength of ~3 kG, though it can range between ~300 G and ~30 kG (e.g. Shultz et al. 2019). As a result, the magnetic threshold selected for these observations is expected to be largely sufficient for the overwhelming majority of targets in this sample. In the case of  $\delta$  Sct stars, however, recent studies suggest that the average field strength might be closer to ~100 G (Thomson-Paressant et al. 2023), and that of  $\gamma$  Dor might be lower than that, since definite detections (DDs) of the latter have yet to be made.

Data taken by ESPaDOnS was reduced using the LIBRESPLIT (Donati et al. 1997) and UPENA (Martoli et al. 2011) pipelines; however, we elected to perform continuum normalisation using the SPENT code (Martin et al. 2017). Spectral line masks were computed using data from the Vienna Atomic Line Database (VALD3, Piskunov et al. 1995; Kupka et al. 1999; Ryabchikova et al. 2015) as a template, based on the stellar parameters of each respective star; namely,  $T_{\text{eff}}$  and  $\log g$ . These template masks were fine-tuned by removing regions coinciding with hydrogen lines, telluric absorption features, and any other features that we considered detrimental to the quality of the spectrum. We then adjusted the line depths of the mask to better match those found in the stellar spectrum, following the standard procedure described in Grunhut et al. (2017). This is particularly important for CP stars, since their line depths differ from those of non-peculiar stars.

Using the least squares deconvolution (LSD) method detailed in Donati et al. (1997), we averaged together the spectral lines and Stokes  $V$  profiles for each target, resulting in an increased signal-to-noise ratio (S/N) with respect to single lines and improved sensitivity to potential magnetic field signatures. This method works by combining the available lines in each spectrum and weighting them with respect to their line depth, Landé factor, and corresponding wavelength. The LSD also generates an  $N$  or ‘null’ profile, which allows one to determine whether the signal in  $V$  is legitimate or spurious.

The LSD Stokes profiles for all the targets in our sample are available for preview and download at <https://zenodo.org/doi/10.5281/zenodo.12745161>

## 4. Results and discussion

Using the LSD Stokes  $V$  and  $I$  profiles generated in the previous step, we calculated the longitudinal field values,  $B_l$ , for each target in our sample (Rees & Semel 1979; Wade et al. 2000). To this end, we defined a region around the centroid of the line such that it includes the full line profile, while limiting the contribution of the continuum. For those stars for which multiple nights

of observation were performed, a  $B_l$  value was calculated for each one. Table A.2 provides the results of this analysis, with the  $B_l$  values appearing in column 8, along with the values for  $N_l$  in column 9, calculated from the  $N$  profiles by applying the same methods used to calculate  $B_l$  from the Stokes  $V$  profiles.

In addition, we applied a false alarm probability (FAP) algorithm to each observation, which determines the probability of there being a signal in Stokes  $V$  in the same velocity region as that used for the  $B_l$  calculations above. The FAP algorithm follows the detection criteria described in Donati et al. (1992), such that a DD requires  $\text{FAP} \leq 10^{-5}$ , a marginal detection (MD) corresponds to  $10^{-5} \leq \text{FAP} \leq 10^{-3}$ , and a non-detection (ND) was determined to apply to values of  $\text{FAP} \geq 10^{-3}$ . Of our sample of 39 stars, 36 had DDs (>92% detection rate) and three had no detections. Of these three, one should not have been included in the initial sample (HD 14251, see Sect. 4.1) and the other two (BD +44 767 and HD 281193) have lower S/N values than required for a DD of a field of at least 300 G, despite large  $B_l$  values. In order to reach our goal threshold of 300 G and check for the presence of a magnetic field, these latter two targets require additional observations. These two stars could thus also be magnetic but our data are of too poor quality to come to a conclusion on this. If we consider only properly selected targets and good quality data, our detection rate is in fact 100%.

Using the determined values for  $B_l$ , we can then calculate the polar field strength using the following equation adapted from Schwarzschild (1950):

$$B_{\text{pol}} = \frac{4(15 - 5u)}{15 + u} \frac{B_l^\pm}{\cos(i \mp \beta)}, \quad (1)$$

where the limb-darkening coefficient,  $u$ , was determined from Claret (2019), based on the surface gravity and effective temperature of the star in question, and  $B_l^+/B_l^-$  correspond to the maximum and minimum amplitudes of a dipolar fit to the  $B_l$  measurements, respectively.

With only one or two observations available for most of the targets presented here, only a minimum value of  $B_{\text{pol}}$  can be inferred. This was done by assuming  $\cos(i \mp \beta) = 1$  and that  $B_l^\pm$  is the maximum or minimum amplitude (based on the sign) of the dipolar fit. As such, should additional longitudinal field measurements become available, the resulting  $B_{\text{pol}}$  can only increase.

The  $B_{\text{pol}}$  values are presented in Table A.2. They range from ~300 G to ~13 kG, which is typical for mCP stars (see e.g. Shultz et al. 2019; Sikora et al. 2019).

In order to establish the S/N required to detect magnetic fields with our desired threshold of 300 G, we required values of  $v \sin i$  for each target, most of which lacked individual spectroscopic studies to determine accurate values for this parameter. As such, the observations were performed utilising a  $v \sin i$  estimate based on the rotational velocity of the star, determined from the precise rotation period from TESS photometric light curves, while assuming  $\sin i = 1$  and an estimated value for the radius of the star. While this works well as a first approximation, and indeed does not significantly impact the quality of our observations for the vast majority of the targets in our sample, it is not a wholly reliable method. In order to accurately calculate  $B_l$  and  $B_{\text{pol}}$ , we elected to determine values of  $v \sin i$  ourselves via the Fourier method. This typically operates by performing a Fourier transform on a number of well-defined and isolated spectral lines, and the position of zeroes present in this Fourier transform provides information on the value of  $v \sin i$  (Simón-Díaz & Herrero 2007). Thanks to the very high-resolution spectra provided by ESPaDOnS and to the nature of the LSD method, we have access to a very well-defined mean

spectral line profile for each star from which we can apply this technique, resulting in a  $v \sin i$  value that is more representative than performing this step on several individual spectral lines. For the few targets that have been the subject of individual studies in the literature, the values we find are consistent with those determined in other works (e.g. Wade 1997), excluding large-scale surveys such as LAMOST in which we found that the determined  $v \sin i$  were largely inaccurate and unreliable. The results of our findings are presented in column 5 of Table A.1.

The results of this study provide many new confirmed magnetic stars that are well suited for additional observations and analysis, and also demonstrate the reliability of using the 5200 Å depression in addition to photometric rotational modulation to identify magnetic candidates. Although the number of pulsating stars in this preliminary sample is limited, with three  $\delta$  Sct (HD 36955, HD 49198, and HD 63843) and one SPB (HD 277595), all of them are confirmed magnetic detections. These magnetic discoveries are significant results, since the sample size of known magnetic pulsating stars is small. There are two more pulsators in our sample awaiting observations. As was mentioned previously, these magnetic pulsating stars are essential for providing better constraints on magneto-astroseismological models and consequently improving our understanding of stellar interiors.

A number of special cases, including the few targets with ND results from the FAP algorithm, those determined to contain stellar companions, as well as any stars presenting pulsations, are detailed in the sections below. In the few cases in which a binary companion was detected and displayed a distinct LSD Stokes  $I$  profile from the primary – that is, SB2 systems – we checked whether a magnetic field could be detected for the secondary. In all such cases, no magnetic field detection was recorded. For these companions, as well as for the three target stars with no field detection listed above, we calculated upper limits of the polar magnetic field strength,  $B_{\text{pol}}$ , determining the maximum value of a magnetic field that might have remained hidden in the noise of the data. The modelling technique utilised for this calculates 1000 oblique dipole models for each of the LSD Stokes  $V$  profiles available for a given target, using random values for the inclination,  $i$ , obliquity angle,  $\beta$ , rotational phase, and a white Gaussian noise with a null average and a variance corresponding to the S/N of each profile (for more information, see Neiner et al. 2015; Thomson-Paressant et al. 2023). We can then calculate the detection rates from these 1000 models and determine the minimum dipolar magnetic field strength that we had a 90% probability of detecting. This is the detectable upper field limit.

A couple of stars appear to also contain binary companions – namely, HD 28238 and HD 49198 – determined through the variation in the LSD Stokes  $I$  profile in one or multiple observations. These targets are thus identified as SB1 systems. We see additional features and variation in the LSD Stokes  $I$  profiles of both HD 212714 and HD 256582; however, in this case the nature of the variations is less clear, and since the  $I$  profiles of the two components are visually indistinct, it makes performing the previously described analysis difficult. We suggest that these features could be the result of rotational effects, or perhaps also SB2 systems.

#### 4.1. HD 14251 – TIC 292977419

HD 14251 was initially flagged as a doubtful CP star during the initial survey of LAMOST targets in Hümmelich et al. (2020); they noted that the star shows enhanced metal-lines but no traditional Si, Cr, Sr, or Eu peculiarities. Through the analysis of the

spectropolarimetric data and the generation of the Stokes profiles<sup>1</sup>, we clearly see a double  $I$  profile characteristic of a spectroscopic binary SB2 system. Neither of the two stars are found to be magnetic, demonstrated by the lack of signal in the Stokes  $V$  profile and the ND result of the FAP algorithm. An upper limit calculation gives values of 2250 and 3000 G at a 90% detection probability for the primary and secondary, respectively, where for the secondary we used a template mask with an adopted  $T_{\text{eff}} = 8500$  K (compared to 12 500 K for the primary) and determined  $v \sin i = 5.44 \pm 2 \text{ km s}^{-1}$  using the Fourier method centred on the LSD Stokes  $I$  profile of the secondary. With these upper field limits, we cannot exclude the possibility that we missed the existence of a magnetic field. However, our analysis shows that this star is an SB2, which may explain the confusion with an mCP star. It is thus likely that HD 14251 is simply a non-magnetic SB2 system.

#### 4.2. *BD+44 767 – TIC 65643991*

Despite a clear and narrow LSD Stokes  $I$  profile<sup>1</sup>, any signal that could be visible in  $V$  is too confounded by noise to be certain, which is confirmed by the ND result of the FAP algorithm. Upper limit calculations suggest we had a 90% probability of detecting a field at least as strong as 1500 G, should one exist. Observations were planned using a  $v \sin i = 7.86 \text{ km s}^{-1}$ , determined from the TESS light curves; however, using the Fourier method in this work we instead determine a value of  $v \sin i = 19 \pm 1 \text{ km s}^{-1}$ , which impacts the S/N required to achieve the 300 G magnetic field threshold and would have subsequently required higher exposure times. As a result, the effectiveness of our observations was negatively impacted by an inaccurately determined value of  $v \sin i$ , which is further confirmed by the 1500 G upper limit value that we determined. Additional observations with a higher S/N would allow us to confirm or deny the existence of a field in this star.

#### 4.3. *HD 281193 – TIC 38555521*

This target presented an ND result from the FAP algorithm, in combination with very large error bars in both  $B_l$  and  $N_l$ . There appears to be a possible hint of signal in  $V$ <sup>1</sup>, but it is not statistically significant. Performing upper limit calculations suggests we had a 90% probability of detecting a field at least as strong as 14 500 G, should one exist, which does not provide much of a restriction. HD 281193 is a relatively fast rotator with  $v \sin i = 103 \pm 3 \text{ km s}^{-1}$  determined via Fourier analysis. The  $v \sin i$  utilised to compute the required S/N for the observations was strongly underestimated, which led to the poor quality of our data and a high upper limit on the detectable field strength. Unfortunately, with such a high  $v \sin i$ , additional spectropolarimetric observations with enough S/N will be difficult to obtain.

#### 4.4. *HD 259273 – TIC 234878810*

This target is a known eclipsing binary (EB) with a 3.409 d orbital period (Labadie-Bartz et al. 2023); however, we clearly observe a signal in the Stokes  $V$  profile after performing LSD, and acquire a DD result from the FAP algorithm. In this case, the magnetic field is clearly aligned on the primary star<sup>1</sup>. The  $N$  profile also shows a signature at the position of the primary component (FAP gives ND and MD, respectively, for the two

sequences), due to the binary radial velocity motion. It is much weaker than in Stokes  $V$  and does not put the magnetic detection into question. However, it may affect the exact  $B_l$  value determined from the Stokes  $V$  profile. Calculating the FAP for the secondary star gives an ND result, and the upper limits algorithm determined a 90% probability of detecting a field with  $B_{\text{pol}} \geq 307$  G. To achieve this, we once again re-calculated the LSD profiles using a template mask with  $T_{\text{eff}} = 8500$  K for the secondary, and determined  $v \sin i = 25 \pm 2 \text{ km s}^{-1}$  from the resulting LSD Stokes  $I$  profile using the Fourier method. For the magnetic primary, we recovered  $v \sin i = 5.1 \pm 2 \text{ km s}^{-1}$ , which was considerably slower than anticipated. Additional information for this system is provided in Appendix B.

#### 4.5. *HD 277595 – TIC 122563793*

Through our spectropolarimetric analysis, HD 277595 has also been identified as an SB2 system, once again demonstrated by the double  $I$  profile in the LSD Stokes profiles<sup>1</sup>. In contradiction to the other SB2 HD 14251, however, HD 277595 is a clear mCP star in Hümmerich et al. (2020) and this time we clearly see a signal in Stokes  $V$ , in the primary star, implying that it is magnetic, which is confirmed by the DD via FAP. We determined a value of  $B_l = 526.7 \pm 120.6$  G, and the FAP shows an ND for the secondary component of the system, confirming that the magnetic field is centred on the primary. Calculating an upper limit value for the secondary, using a  $T_{\text{eff}} = 8500$  K template mask and calculating  $v \sin i = 9.42 \pm 1 \text{ km s}^{-1}$  (compared to 12 500 K and  $13 \pm 1 \text{ km s}^{-1}$  for the primary), we determine that we had a 90% probability of detecting a field at least as strong as 1866 G in the secondary component.

In addition, SPB pulsations were observed in the TESS light curves, which appear to coincide with the magnetic primary, especially considering the B8VSi spectral type and the comparatively cool secondary. The primary component of HD 277595 is thus a new magnetic SPB star.

#### 4.6. *HD 36955 – TIC 427377135*

HD 36955 displays multiple  $\delta$  Sct pulsations between 30 and  $50 \text{ d}^{-1}$ , with an additional peak at  $18.5 \text{ d}^{-1}$  (see Fig. B.1). Through the analysis of the spectropolarimetric data, we determine a clear magnetic detection, with  $B_l = -580.6 \pm 60$  G, corresponding to an approximate polar magnetic field strength of the order of  $B_{\text{pol}} \geq 1850$  G, assuming a dipolar field structure. HD 36955 is thus a new magnetic  $\delta$  Sct star.

#### 4.7. *HD 63843 – TIC 35884762*

We observe  $\delta$  Sct pulsations in this star with frequencies between 9 and  $22 \text{ d}^{-1}$  (see Fig. B.1). As with the previous star, we detect a clear magnetic field with  $B_l = 2191.3 \pm 15$  G and, assuming a dipolar field structure,  $B_{\text{pol}} \geq 6600$  G. HD 63843 is thus another new magnetic  $\delta$  Sct star.

#### 4.8. *HD 49198 – TIC 16485771*

Amongst our sample of stars, one target in particular received more observations than the others: HD 49198. This was as a result of it being a relatively bright target, displaying clear  $\delta$  Sct pulsations between about 12 and  $38 \text{ d}^{-1}$  (see Fig. B.1), and having a clear, well-defined magnetic detection during the first semester (see Fig. 2), making it a new magnetic  $\delta$  Sct star and a

<sup>1</sup> See <https://zenodo.org/doi/10.5281/zenodo.12745161>

particularly appealing target for this study. It is also an SB1, as is evidenced by the shift in the Stokes  $I$  profile<sup>1</sup>. The multiple observations allowed us to perform additional analysis for this star, and infer the overall characterisation of the magnetic field.

First, the  $B_l$  values that we calculated for this star were significantly higher than those for almost any other targets in our sample, with very small error bars. Using these values in combination with the rotational period, inferred by TESS photometry, we can visualise the evolution of the longitudinal magnetic field with respect to the rotation of the star, seen in Fig. 3. Fitting a simple sinusoidal function to the data points, to approximate the variation in a dipolar field, we see that the fit is extremely representative ( $\chi^2 = 0.305$ ). Such a low  $\chi^2$  means we are probably overestimating the error bars on the  $B_l$  values. It is therefore safe to assume that the magnetic field of HD 49198 is dipolar in nature, with a strength varying between

$$\begin{cases} B_l^+ = -785.5 \pm 32.6 \text{ G} \\ B_l^- = -3,212.2 \pm 32.6 \text{ G}. \end{cases}$$

Assuming that the field is indeed dipolar, we can derive the polar field strength,  $B_{\text{pol}}$ , and the magnetic field obliquity,  $\beta$ . First, we need to calculate the inclination of the rotational axis of the star with respect to the line of sight. For this, we followed the method detailed in various other articles (e.g. Fréour et al. 2022; Thomson-Paressant et al. 2020), utilising an oblique rotator model first defined by Stibbs (1950), to determine a value for  $i$ , then for  $\beta$  and  $B_{\text{pol}}$ . Using the values from Gaia (Gaia Collaboration 2023) for the effective temperature,  $T_{\text{eff}} = 9839 \pm 220 \text{ K}$ , and absolute magnitude,  $M = 0.72 \pm 0.09$ , the value from TESS for the rotation period,  $P_{\text{rot}} = 6.2237647 \text{ d}$ , inferring the rotational velocity,  $v \sin i = 14.97 \pm 1 \text{ km s}^{-1}$ , using the Fourier method on the LSD Stokes  $I$  profile, as well as the radius-luminosity-temperature relation (Eq. (3)), we can calculate a value for the inclination:

$$\frac{L}{L_{\odot}} = 2.51^{(4.83-M)} \quad (2)$$

$$\frac{R}{R_{\odot}} = \left(\frac{T}{T_{\odot}}\right)^{-2} \left(\frac{L}{L_{\odot}}\right)^{1/2} \quad (3)$$

$$i = \sin^{-1} \left( \frac{v \sin i P_{\text{rot}}}{2\pi R} \right). \quad (4)$$

We determined values of  $L = 43.92 \pm 3.64 L_{\odot}$ ,  $R = 2.29 \pm 0.14 R_{\odot}$ , and  $i = 53 \pm 7^{\circ}$  for the luminosity, radius, and inclination, respectively. Using this value for  $i$  in combination with the ratio between the minimum and maximum longitudinal field values, we could then determine a value for  $\beta$  with respect to the inclination (Preston 1967):

$$\frac{B_{l,\text{min}}}{B_{l,\text{max}}} = \frac{\cos(i + \beta)}{\cos(i - \beta)}. \quad (5)$$

In our case, utilising the values for  $i$ ,  $B_l^+$ , and  $B_l^-$  defined above, we find that  $\beta = 155 \pm 5^{\circ}$ . Finally,  $B_{\text{pol}}$  can be estimated utilising Eq. (1) above, taken from Schwarzschild (1950), where we have assumed a limb-darkening coefficient of  $u = 0.5044$ , determined from Claret (2019). Using the calculated values for  $i$ ,  $\beta$ , and  $B_l$ , we determine that  $B_{\text{pol}} = 11\,740 \pm 2700 \text{ G}$ . The error on this value is limited by our precision on  $i$  and subsequently  $\beta$ .

In Fig. 3, we see that the maximum of the folded light curve (top panel) is slightly shifted with respect to the minimum of the longitudinal field curve (bottom panel). This is often observed in CP stars in which chemical spots are close to the magnetic pole but not right on it.

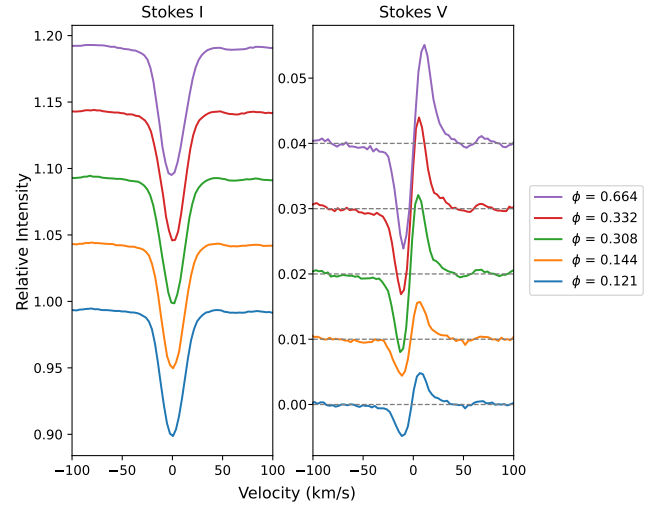


**Fig. 2.** Stokes  $I$  (left panel) and  $V$  (right panel) profiles for HD 49198, ordered with respect to the rotational phase of the star and shifted vertically for clarity. The zero-points for each respective Stokes  $V$  profile has been defined by a dashed line.

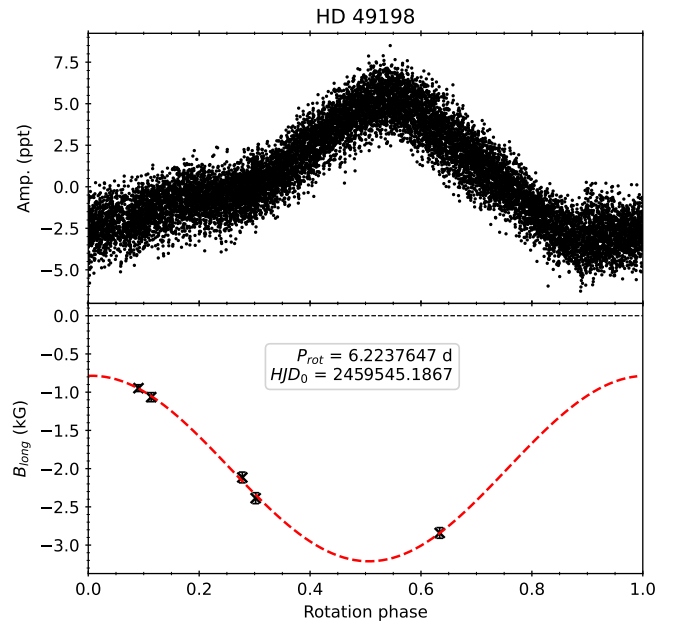


**Fig. 3.** TESS photometric light curve of HD 49198 (top panel), phase-folded with respect to the rotation period, utilising data from all currently available sectors (s20, s60, and s73). Longitudinal magnetic field values (bottom panel) for HD 49198 with their respective error bars, phase-folded with respect to the rotation period and overplotted with a simple dipolar fit. The values for the rotation period ( $P_{\text{rot}}$ ) and initial heliocentric Julian date ( $\text{HJD}_0$ ) are provided for reference.

This kind of in-depth analysis is most beneficial when working with numerous exposures, as it allows us to better constrain the polar field strength value and its structure, taking pulsations into account. By acquiring additional observations of this star covering the rotation and pulsation phases, we will be able to perform Zeeman-Doppler imaging (ZDI; Folsom et al. 2017), allowing us to model and characterise the magnetic field at the surface of the star.

## 5. Conclusions

Of our sample of 39 candidates, we determined 36 of them to be clearly magnetic, with only one likely non-magnetic one and a couple requiring better data in order for their magnetic statuses to be checked. Thus, a large number of confirmed mCP stars have been determined and are suitable for in-depth follow-up and analysis. In particular, three new magnetic  $\delta$  Sct stars and one new magnetic SPB star have been discovered in this work. This is an extremely promising result for the study of stellar magnetism.

This study also proves the viability of the method formalised by Hümmerich et al. (2020), using the 5200 Å depression combined with rotational modulation as a reliable indicator of the presence of a magnetic field in CP stars. This is a key result, one that can be utilised to generate large lists of candidate mCP stars with very high chances of detecting fields in all of them.

The magnetic pulsating stars determined as a result of this analysis are essential targets for follow-up observations and subsequent magneto-asteroseismic analysis. Such magnetic pulsating hot stars are rare and our discoveries, while few in number, still provide a large increase in targets in this category. Again, thanks to the reliability of the detection method, all targets that fall in the area overlapped by both chemical peculiarity and pulsation can be quickly and efficiently assessed for the presence of the 5200 Å depression and rotational modulation and, with a high likelihood, a magnetic field.

*Acknowledgements.* We thank S. Hummerich for providing a spreadsheet version of the table in Hümmerich et al. (2020) before publication of his paper. This work is based on observations obtained at the Canada-France-Hawaii Telescope (CFHT) which is operated by the National Research Council (NRC) of Canada, the Institut National des Sciences de l'Univers of the Centre National de la Recherche Scientifique (CNRS) of France, and the University of Hawaii. This research has made use of the SIMBAD database operated at CDS, Strasbourg (France), and of NASA's Astrophysics Data System (ADS). This paper includes data collected by the TESS mission, which are publicly available from the Mikulski Archive for Space Telescopes (MAST). Funding for the TESS mission is provided by NASA's Science Mission directorate.

## References

- Alecian, G. 1986, in *Upper Main Sequence Stars with Anomalous Abundances*, eds. C. R. Cowley, M. M. Dworetzky, & C. Mégessier (Dordrecht: Springer), 381
- Aurière, M., Wade, G. A., Silvester, J., et al. 2007, *A&A*, 475, 1053
- Babcock, H. W. 1960, *ApJ*, 132, 521
- Buysschaert, B., Neiner, C., Martin, A. J., et al. 2018, *MNRAS*, 478, 2777
- Claret, A. 2019, *VizieR Online Data Catalog: VI/154*
- Cui, X.-Q., Zhao, Y.-H., Chu, Y.-Q., et al. 2012, *RAA*, 12, 1197
- Donati, J.-F., & Landstreet, J. 2009, *ARA&A*, 47, 333
- Donati, J. F., Brown, S. F., Semel, M., et al. 1992, *A&A*, 265, 682
- Donati, J. F., Semel, M., Carter, B. D., Rees, D. E., & Collier Cameron, A. 1997, *MNRAS*, 291, 658
- Donati, J. F., Catala, C., Landstreet, J. D., & Petit, P. 2006, *ASP Conf. Ser.*, 358, 362
- Ferrario, L., Melatos, A., & Zrake, J. 2015, *Space Sci. Rev.*, 191, 77
- Folsom, C. P., Bouvier, J., Petit, P., et al. 2017, *MNRAS*, 474, 4956
- Fossati, L., Castro, N., Schöler, M., et al. 2015, *A&A*, 582, A45
- Fréour, L., Neiner, C., Landstreet, J. D., Folsom, C. P., & Wade, G. A. 2022, *MNRAS*, 520, 3201
- Gaia Collaboration (Vallenari, A., et al.) 2023, *A&A*, 674, A1
- Grunhut, J. H., Wade, G. A., Neiner, C., et al. 2017, *MNRAS*, 465, 2432
- Hümmerich, S., Mikulášek, Z., Paunzen, E., et al. 2018, *A&A*, 619, A98
- Hümmerich, S., Paunzen, E., & Bernhard, K. 2020, *A&A*, 640, A40
- Khan, S. A., & Shulyak, D. V. 2007, *A&A*, 469, 1083
- Kochukhov, O. 2009, *Commun. Asteroseismol.*, 159, 61
- Kupka, F., Piskunov, N., Ryabchikova, T. A., Stempels, H. C., & Weiss, W. W. 1999, *A&AS*, 138, 119
- Kupka, F., Paunzen, E., & Maitzen, H. M. 2003, *MNRAS*, 341, 849
- Kupka, F., Paunzen, E., Iliev, I. K., & Maitzen, H. M. 2004, *MNRAS*, 352, 863
- Kurtz, D. W. 2022, *ARA&A*, 60, 31
- Labadie-Bartz, J., Hümmerich, S., Bernhard, K., Paunzen, E., & Shultz, M. E. 2023, *A&A*, 676, A55
- Landstreet, J. D. 1982, *ApJ*, 258, 639
- Lenz, P., & Breger, M. 2005, *Commun. Asteroseismol.*, 146, 53
- Maitzen, H. M. 1976, *A&A*, 51, 223
- Martin, A. J., Neiner, C., Oksala, M. E., et al. 2017, *MNRAS*, 475, 1521
- Martiooli, E., Teple, D., & Manset, N. 2011, in *Telescopes from Afar*, eds. S. Gajadhar, J. Walawender, R. Genet, et al., 63
- Michaud, G. 1970, *ApJ*, 160, 641
- Neiner, C., Grunhut, J., Leroy, B., De Becker, M., & Rauw, G. 2015, *A&A*, 575, A66
- Piskunov, N. E., Kupka, F., Ryabchikova, T. A., Weiss, W. W., & Jeffery, C. S. 1995, *A&AS*, 112
- Preston, G. W. 1967, *ApJ*, 150, 547
- Preston, G. W. 1974, *ARA&A*, 12, 257
- Rees, D. E., & Semel, M. D. 1979, *A&A*, 74, 1
- Ricker, G. R., Winn, J. N., Vanderspek, R., et al. 2015, *J. Astron. Telesc. Instrum. Syst.*, 1, 014003
- Ryabchikova, T., Piskunov, N., Kurucz, R. L., et al. 2015, *Phys. Scr.*, 90, 054005
- Schwarzschild, M. 1950, *ApJ*, 112, 222
- Shultz, M. E., Wade, G. A., Rivinius, T., et al. 2019, *MNRAS*, 490, 274
- Sikora, J., Wade, G. A., Power, J., & Neiner, C. 2019, *MNRAS*, 483, 3127
- Simón-Díaz, S., & Herrero, A. 2007, *A&A*, 468, 1063
- Stibbs, D. W. N. 1950, *MNRAS*, 110, 395
- Stigler, C., Maitzen, H. M., Paunzen, E., & Netopil, M. 2014, *A&A*, 562, A65
- Thomson-Paressant, K., Neiner, C., Zwintz, K., & Escorza, A. 2020, *MNRAS*, 500, 1992
- Thomson-Paressant, K., Neiner, C., Lampens, P., et al. 2023, *MNRAS*, 526, 1728
- Wade, G. A. 1997, *A&A*, 325, 1063
- Wade, G. A., Donati, J.-F., Landstreet, J. D., & Shorlin, S. L. S. 2000, *MNRAS*, 313, 851
- Wolff, S. C. 1968, *PASP*, 80, 281
- Zhang, B., Jing, Y.-J., Yang, F., et al. 2022, *ApJS*, 258, 26
- Zhao, G., Zhao, Y.-H., Chu, Y.-Q., Jing, Y.-P., & Deng, L.-C. 2012, *RAA*, 12, 723

## Appendix A: Tables

Table A.1. Summary of observational parameters for the targets in our sample.

Target	TIC	Spectral Type	Vmag	Date	Mid-HJD +2459000	T <sub>exp</sub> (seqx4xs)
BD +00 2099	271310339	kB8hA3mA3CrEu	9.90	23-Feb-21	269.95	1x4x519
BD +01 1920	271375640	A1III-IVSrSiEu	10.02	07-Jan-24	1318.0421	1x4x206
BD +08 2211	312111544	kA3hA5mA7SiEu	9.81	04-Jan-24	1315.1807	1x4x220
BD +10 2572	404536886	kA3hA7mA9SrCrEu	9.75	21-Feb-21	633.0596	1x4x133
BD +40 4697	305482510	B9III-IVSi	9.75	18-May-21	354.1158	1x4x276
BD +43 3648	188301298	kB9hA0mA2Si	9.57	18-May-21	354.1043	1x4x177
BD +44 767	65643991	kA0hA1mA3(Si)	9.90	25-Nov-21	544.7399	1x4x73
BD +49 1011	428515156	B8IV-VCrSi	9.71	26-Nov-21	545.7688	1x4x128
HD 11140	72150546	B8IVSi	8.56	01-Sept-21	459.9184	1x4x94
HD 14251	292977419	B8IV-V	9.43	30-Aug-21	457.96	1x4x538
HD 18410	251412475	kB7hA7mA6CrEuSi	9.14	01-Sept-21	459.9253	2x4x67
HD 19846	445923870	B9IV-VEu	8.57	25-Nov-21	544.7592	1x4x359
HD 22961	284084463	A0IV-VSi	9.57	26-Nov-21	545.785	1x4x465
HD 28238	373024953	A2IV-VSrCrEu	9.16	28-Aug-21	456.1498	1x4x24
				26-Nov-21	545.8317	1x4x24
HD 36259	268068786	B8IVSi	9.08	01-Sept-21	460.0312	1x4x878
HD 36955	427377135	kA0hA2mA4CrEu	9.58	01-Sept-21	460.0706	1x4x656
HD 48560	11767386	kA1hA2mA5CrEu	9.60	27-Nov-21	547.0746	1x4x93
HD 49198	16485771	A0III-IVCrSi	9.31	26-Nov-21	545.8924	1x4x319
				27-Nov-21	547.0635	1x4x319
				18-Feb-22	629.9653	1x4x319
				21-Feb-22	632.8058	1x4x319
				22-Feb-22	633.9703	1x4x319
HD 49522	91136550	A0VCrEuSi	8.88	23-Feb-21	269.9116	1x4x316
HD 56514	440829763	A5IV-VSrCrEu	9.36	23-Feb-21	269.9287	1x4x266
HD 63843	35884762	A2IVSrSi	10.25	18-Jan-24	1329.0059	1x4x280
HD 66533	169971995	kB9hA3mA8SrCrEu	9.44	27-Nov-21	547.1427	1x4x32
HD 71047	27256691	A5III-IVSr	9.60	23-Feb-21	269.9804	1x4x299
HD 86170	62815493	kA2hA3mA6SrCrEu	8.41	23-Feb-21	269.9932	1x4x30
HD 108662	393808105	B9VCrEu	5.24	20-May-21	355.9027	2x4x30
				21-May-21	356.8757	1x4x30
HD 177128	120495323	kA1hA4mA6SrCrEu	9.11	18-May-21	353.9324	1x4x100
HD 212714	164282311	B8IVEuSi	8.72	18-Jul-22	779.8864	1x4x1008
HD 232285	240808702	B9VCrEuSi	9.42	30-Aug-21	457.8978	1x4x147
HD 256582	319616512	B5VHeB9	10.01	22-Feb-22	633.8106	2x4x1434
HD 259273	234878810	B9III-IVSi	9.73	25-Dec-21	574.8461	2x4x937
HD 266267	235391838	A9VrSiEu	10.04	15-Jan-24	1326.0506	1x4x55
HD 266311	237662091	kA1hA3mA6SrCrEu	9.74	23-Feb-21	269.9003	1x4x40
HD 277595	122563793	B8VSi	9.55	01-Sept-21	459.9937	2x4x200
HD 281193	385555521	A4IVCrEuSi	10.08	25-Nov-21	544.7461	1x4x89
TYC 2873-3205-1	384988765	B9.5VSi	9.98	01-Sept-21	459.9566	1x4x546
TYC 3316-892-1	458780077	B9IV-VSi	9.74	25-Nov-21	544.7318	1x4x186
TYC 3319-464-1	117663254	B9.5IV-VCrEu	9.74	01-Sept-21	459.9384	1x4x146
TYC 3733-133-1	252212077	A2IVCrEu	9.66	26-Nov-21	545.8352	1x4x40
TYC 3749-888-1	321832920	A7VrCrEuSi	9.81	27-Nov-21	545.8406	1x4x73

**Notes.** Column 3 provides the spectral type from [Hümmerich et al. \(2020\)](#) and column 4 presents the apparent V magnitude. Observation dates are provided in two formats in columns 6 and 7, with the number of sequences (seq) and exposure times in seconds in column 8.



**Table A.2.** Results of magnetic characterisation of our sample.

Target	Date	Mn $\lambda$ (nm)	Mn Landé	S/N	$v \sin i$ (km s <sup>-1</sup> )	$u$	FAP	$B_l \pm \sigma B$ (G)	$N_l \pm \sigma N$ (G)	$B_{\text{pol}} \pm \sigma B$ or $B_{\text{lim}}$ (G)
BD +00 2099	23-Feb-21	536.7149	1.202	1537	24 ± 1	0.5443	DD	-521 ± 35	34 ± 34	> 1646 ± 111
BD +01 1920	07-Jan-24	529.6655	1.208	913	5 ± 1	0.5443	DD	-416 ± 7	-9 ± 6	> 1314 ± 22
BD +08 2211	04-Jan-24	537.8177	1.199	943	6 ± 1	0.5751	DD	152 ± 13	20 ± 7	> 474 ± 40
BD +10 2572	21-Feb-21	540.0438	1.189	1683	10 ± 3	0.5751	DD	-1268 ± 26	10 ± 20	> 3948 ± 82
BD +40 4697	18-May-21	535.3467	1.197	1137	18 ± 1	0.4444	DD	3898 ± 60	16 ± 37	> 12,900 ± 200
BD +43 3648	18-May-21	531.1814	1.205	1520	17 ± 1	0.5046	DD	-2021 ± 106	6 ± 92	> 6504 ± 341
BD +44 767	25-Nov-21	555.8105	1.199	1213	18 ± 1	0.5151	ND	453 ± 192	-40 ± 193	< 1500
BD +49 1011	26-Nov-21	543.1386	1.192	801	7 ± 1	0.4249	DD	-279 ± 38	-35 ± 37	> 934 ± 128
HD 11140	01-Sept-21	533.8171	1.191	2174	21 ± 1	0.4249	DD	206 ± 70	82 ± 70	> 690 ± 234
HD 14251a	30-Aug-21	532.7064	1.191	3416	40 ± 1	0.4249	ND	142 ± 152	82 ± 152	< 2250
HD 14251b					5 ± 2		ND	2 ± 89	-35 ± 89	< 3000
HD 18410	01-Sept-21	542.0123	1.192	1478	21 ± 1	0.5751	DD	1867 ± 39	-7 ± 34	> 5814 ± 121
HD 19846	25-Nov-21	528.7895	1.197	1360	27 ± 1	0.4444	DD	194 ± 50	-48 ± 35	> 642 ± 165
HD 22961	26-Nov-21	529.6589	1.205	1839	18 ± 1	0.5046	DD	102 ± 38	45 ± 38	> 328 ± 124
HD 28238	28-Aug-21	537.5226	1.206	747	6 ± 1	0.5279	DD	-207 ± 17	0 ± 16	> 684 ± 55
	26-Nov-21	536.1829	1.207	822			DD	1 ± 18	17 ± 18	
HD 36259	01-Sept-21	533.7634	1.191	2190	28 ± 1	0.4249	DD	761 ± 19	-1 ± 17	> 2548 ± 63
HD 36955	01-Sept-21	526.764	1.208	1855	33 ± 1	0.5279	DD	-581 ± 60	35 ± 58	> 1849 ± 191
HD 48560	27-Nov-21	529.8405	1.207	1466	8 ± 2	0.5279	DD	-932 ± 30	14 ± 28	> 2967 ± 94
HD 49198	26-Nov-21	525.9691	1.206	1459	15 ± 1	0.5044	DD	-1065 ± 59	-56 ± 50	11,740 ± 2700
	27-Nov-21	524.039	1.206	1394			DD	-2386 ± 72	-26 ± 41	
	18-Feb-22	527.567	1.205	1220			DD	-2841 ± 70	-50 ± 38	
	21-Feb-22	523.3311	1.206	1454			DD	-947 ± 44	41 ± 35	
	22-Feb-22	528.355	1.205	1392			DD	-2115 ± 70	40 ± 45	
HD 49522	23-Feb-21	526.4611	1.205	1221	22 ± 1	0.5046	DD	-2353 ± 25	-7 ± 16	> 7573 ± 80
HD 56514	23-Feb-21	531.4868	1.216	2027	32 ± 1	0.5765	DD	-256 ± 54	1 ± 53	> 795 ± 168
HD 63843	18-Jan-24	526.345	1.189	1708	7 ± 2	0.5659	DD	2191 ± 15	5 ± 10	> 6853 ± 47
HD 66533	27-Nov-21	532.1027	1.197	906	15 ± 1	0.5443	DD	-282 ± 19	-17 ± 18	> 889 ± 59
HD 71047	23-Feb-21	525.6292	1.199	1816	16 ± 1	0.5765	DD	165 ± 28	-1 ± 25	> 516 ± 88
HD 86170	23-Feb-21	534.0372	1.197	924	5 ± 2	0.5443	DD	-104 ± 26	-16 ± 24	> 328 ± 83
HD 108662	20-May-21	534.5184	1.195	1394	20 ± 1	0.4444	DD	-690 ± 73	8 ± 73	> 2283 ± 243
	21-May-21	527.9288	1.197	1118			DD	-5 ± 22	-32 ± 20	
HD 177128	18-May-21	527.0712	1.200	1452	19 ± 1	0.5630	DD	860 ± 58	-67 ± 54	> 2693 ± 183
HD 212714	18-Jul-22	543.2427	1.181	2961	59 ± 7	0.4249	DD	-114 ± 38	-8 ± 38	> 380 ± 128
HD 232285	30-Aug-21	534.9881	1.197	925	7 ± 1	0.4444	DD	771 ± 17	12 ± 13	> 2553 ± 56
HD 256582	22-Feb-22	566.5622	1.197	3907	45 ± 1	0.3749	DD	-154 ± 74	-24 ± 73	> 526 ± 253
HD 259273a	25-Dec-21	528.9497	1.197	2452	5 ± 2	0.4444	DD	-144 ± 8	0 ± 8	> 449 ± 26
HD 259273b					25 ± 2		ND	-2000 ± 990	538 ± 824	< 307
HD 266267	15-Jan-24	540.7631	1.208	919	5 ± 3	0.5765	DD	403 ± 11	27 ± 11	> 1254 ± 35
HD 266311	23-Feb-21	539.0441	1.196	767	8 ± 1	0.5443	DD	-1347 ± 21	-32 ± 18	> 4256 ± 65
HD 277595a	01-Sept-21	539.4005	1.191	3635	13 ± 1	0.4249	DD	527 ± 121	13 ± 120	> 1764 ± 404
HD 277595b					9 ± 1		ND	20 ± 121	-7 ± 121	< 1866
HD 281193	25-Nov-21	537.4729	1.206	2296	104 ± 2	0.5630	ND	628 ± 321	-638 ± 322	< 14,500
TYC 2873-3205-1	01-Sept-21	526.6307	1.201	1815	18 ± 1	0.4724	DD	213 ± 35	-1 ± 35	> 697 ± 114
TYC 3316-892-1	25-Nov-21	538.0924	1.197	1648	18 ± 1	0.4444	DD	965 ± 57	-55 ± 53	> 3192 ± 187
TYC 3319-464-1	01-Sept-21	542.2375	1.198	614	7 ± 1	0.4444	DD	280 ± 22	13 ± 19	> 925 ± 72
TYC 3733-133-1	26-Nov-21	548.7484	1.197	754	9 ± 1	0.5279	DD	-1127 ± 30	-13 ± 24	> 3589 ± 96
TYC 3749-888-1	27-Nov-21	555.074	1.188	2043	25 ± 1	0.5751	DD	-458 ± 63	-47 ± 62	> 1425 ± 196

**Notes.** Columns 3, 4, and 5 display the mean values for wavelength and Landé factor, and S/N for the LSD I profiles respectively. In the case of multiple sequences during a single night, these values were averaged together. Our Fourier-method determined values for  $v \sin i$  are presented in column 6, along with in column 7 the determined limb-darkening coefficients  $u$  (Claret 2019) for  $B_{\text{pol}}$  calculations. The results of the FAP algorithm are shown in column 8, and the longitudinal field measurements from the Stokes V ( $B_l$ ) and the corresponding N ( $N_l$ ) profiles, with their respective errors, are provided in columns 9 and 10. Finally, values for the polar field strength  $B_{\text{pol}}$  and their errors when a magnetic field was detected or the upper limit  $B_{\text{lim}}$  for NDs are presented in column 11. The  $B_{\text{pol}}$  values for targets having only one or two polarimetric sequences are lower bounds, and have been represented as such.

## Appendix B: TESS frequency spectra

We revisited the *TESS* data for the four pulsators and one EB of this sample, including more recent data than was presented in [Labadie-Bartz et al. \(2023\)](#) whenever available. For the three  $\delta$  Sct pulsators, it is important to ensure that the stellar oscillation frequencies are below the Nyquist frequency of the *TESS* photometry. Only one of these, HD 36955 (TIC 427377135), had 2-minute cadence data (from sector 6), so we largely rely on the full frame images (FFIs). The cadence of the FFIs has increased since the start of the mission, resulting in higher Nyquist frequencies and thus the ability to detect higher frequency signals. In the first two *TESS* cycles (sectors 1 to 26), the FFI cadence was 30 minutes (Nyquist frequency of  $24 \text{ d}^{-1}$ ), in the next two cycles (sectors 27 to 55) the FFI cadence was 10 minutes (Nyquist frequency of  $72 \text{ d}^{-1}$ ), and in cycle 56 and later the FFI cadence was increased to 200 seconds (Nyquist frequency of  $216 \text{ d}^{-1}$ ).

The frequency spectra are plotted in Fig. B.1, computed using Period04 ([Lenz & Breger 2005](#)). First the rotational frequency and any harmonics were removed, and subsequent peaks were identified through iterative pre-whitening and a simultaneous fit of all significant peaks (above a S/N threshold of 4, using a  $2 \text{ d}^{-1}$  window centred on each signal). Inspection of the highest-cadence *TESS* light curve available for these targets (2-minute cadence for HD 36955, and 200 second cadence for the rest) did not show any significant peaks beyond what is plotted in Fig. B.1, demonstrating that the 10-minute cadence data do not suffer from super-Nyquist aliasing (although the amplitude of the highest frequency peaks for HD 36955 may be slightly suppressed in the sector 32 data). The frequency spectrum in Fig. B.1 for HD 49198 supersedes what is shown in [Labadie-Bartz et al. \(2023\)](#) which relied on 30-minute cadence data (and so did suffer from super-Nyquist aliasing).

*HD 277595*: The low-frequency group of signals centred around  $1.5 \text{ d}^{-1}$  is poorly resolved, and it is unclear as to whether or not there are genuine differences between sectors 19 and 59, or if the perceived differences are due to insufficient frequency resolution. However, the difference in the signals lower than  $0.5 \text{ d}^{-1}$  do seem genuine. Considering the spectral type (B8VSi), the photometric variations are consistent with SPB pulsation.

*HD 49198*: The frequency spectrum is similar when comparing sectors 60 and 73, with some changes in the relative strength of a few signals. The observed behaviour is typical for  $\delta$  Scuti pulsators.

*HD 63843*: There are significant differences in the relative amplitude of signals that are strong in one or both sectors (e.g. at  $19.7 \text{ d}^{-1}$  and  $16.7 \text{ d}^{-1}$ ). Two higher frequency signals, at  $26.5$  and  $26.8 \text{ d}^{-1}$  only appear prominently in sector 61. These signals are typical of  $\delta$  Scuti pulsators.

*HD 36955*: The frequency spectra are similar in sectors 6 and 32 for the high frequency  $\delta$  Scuti pulsation, but with some relative changes in amplitude. The lower frequency signals ( $< 2 \text{ d}^{-1}$ ) change between sectors and possibly reflect  $\gamma$  Dor pulsation, although this is not entirely clear.

*HD 259273*: We re-visited the *TESS* photometry for this EB considering the information gleaned from our analysis of the ESPaDOnS data. In [Labadie-Bartz et al. \(2023\)](#), the rotation period of the magnetic star was presumed to be the same as that of the orbital period (3.409073 d), due to the unambiguous nature of the eclipses and the coherent out-of-eclipse variability consistent with rotation. However, from the very narrow Stokes I line profile for the magnetic component<sup>2</sup> we measured  $v \sin i = 5.1 \pm 2 \text{ km s}^{-1}$ . Coarsely estimating the radius of the magnetic star to be between 2 and  $3 R_{\odot}$  (consistent with its late B spectral type), considering the uncertainty on  $v \sin i$ , and setting  $i = 90^{\circ}$ , the rotation period should be between about 14 and 50 days – considerably slower than the orbital period and the out-of-eclipse variability. A more careful extraction of the two sectors of available *TESS* data revealed a slow oscillation with a 15.5 day period, as shown by the red curves in Fig. B.2, which may be caused by rotation of the magnetic star. Future additional spectropolarimetry can be used to unambiguously determine the rotation period. The secondary is more broad lined with  $v \sin i = 5.1 \pm 2 \text{ km s}^{-1}$ , where a radius of  $1.5 (2.0) R_{\odot}$  and  $i = 90^{\circ}$  corresponds to a rotation period of 3.0 (4.0) d, and thus may be tidally locked.

After subtracting the slow oscillation, the same photometry phased to the orbital period is shown in Fig. B.3 along with the RV measurements for both components determined from the Stokes I profile<sup>2</sup>, and one RV measurement of the primary (magnetic) star from LAMOST DR8 ([Zhang et al. 2022](#)). Although the RV measurements are sparse, they suggest that the magnetic star is a genuine member of the eclipsing pair (and not, e.g., a further out tertiary), and that it is the hotter component. Since the magnetic star seems to rotate much slower than the orbital period, it is not tidally locked (but the secondary may be). A rotating secondary can only explain the variation if it has surface features that are stable for at least as long as the *TESS* observing baseline ( $\sim 2$  years). Magnetism can cause such spots, but no magnetic field was detected in the secondary (Sec. 4.4). The out-of-eclipse variation is then perhaps best explained by a reflection effect where the hotter primary irradiates the primary-facing hemisphere of the secondary. The orbit appears to not be perfectly circular, as the secondary eclipse occurs at 0.510 in phase after the primary eclipse. From the RV semi-amplitudes and the relative eclipse depths, the secondary should be  $\sim 0.77$  times the mass of the primary, and  $\sim 0.9$  times the effective temperature of the primary (consistent with an early to mid A star). Further data and analysis are required to properly characterise the stellar and binary properties of this system, but the information presented here provides a useful starting point.

The radial velocity measurements (determined from a Gaussian fit) from the two Stokes I profiles for HD 259273 are  $87.56 \pm 0.05 \text{ km s}^{-1}$  and  $-119.08 \pm 0.5 \text{ km s}^{-1}$  for the primary and secondary components, respectively, for the observation taken at MJD = 2459574.846135, and  $83.62 \pm 0.05 \text{ km s}^{-1}$  and  $-114.99 \pm 0.5 \text{ km s}^{-1}$  for the observation at MJD = 2459574.892165.

<sup>2</sup> See [10.5281/zenodo.12745161](https://doi.org/10.5281/zenodo.12745161)

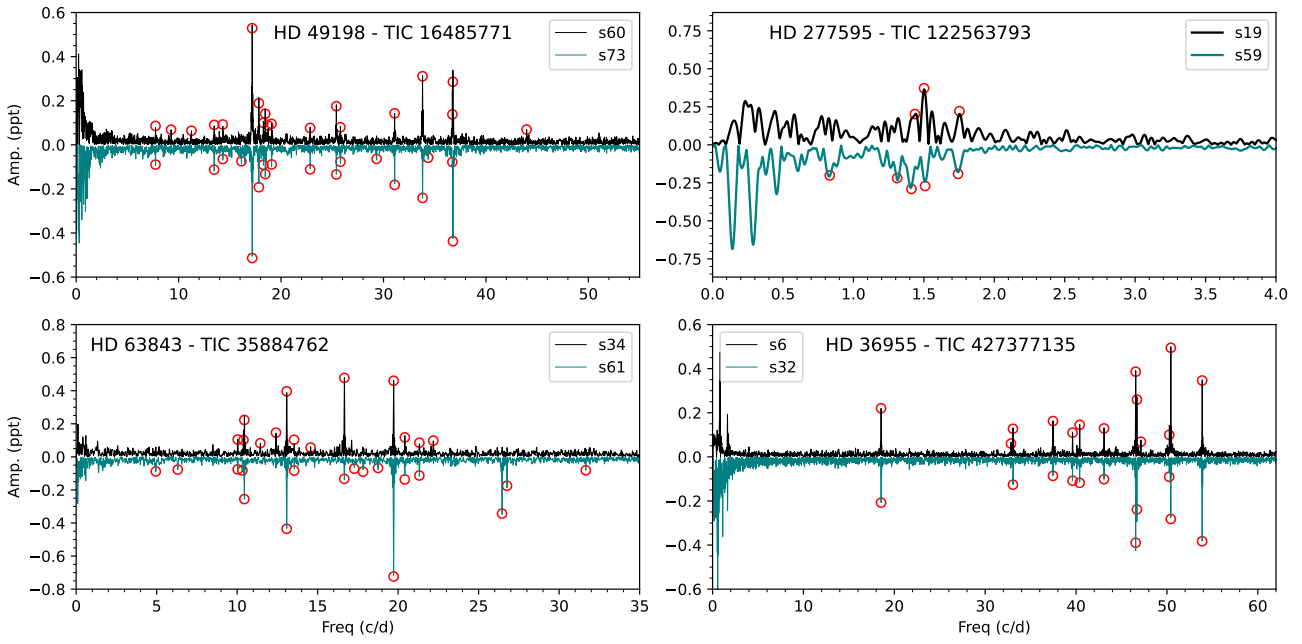


**Fig. B.1.** *TESS* frequency spectra for the four pulsators after removing the rotational signal (except for HD 63843 which does not show detectable rotational modulation in the *TESS* data), computed from two different sectors of data for each star (the curve for the latter sector is inverted). Individual frequencies are marked with red circles.

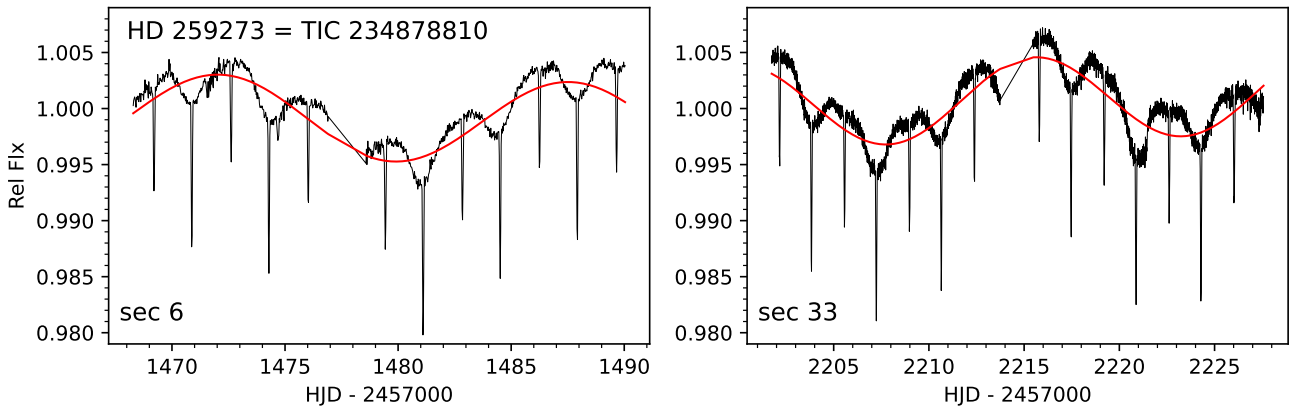


**Fig. B.2.** *TESS* light curves of HD 259273 from sectors 6 and 33. The red curve shows the 15.5 day signal that is potentially associated with rotation of the magnetic star.

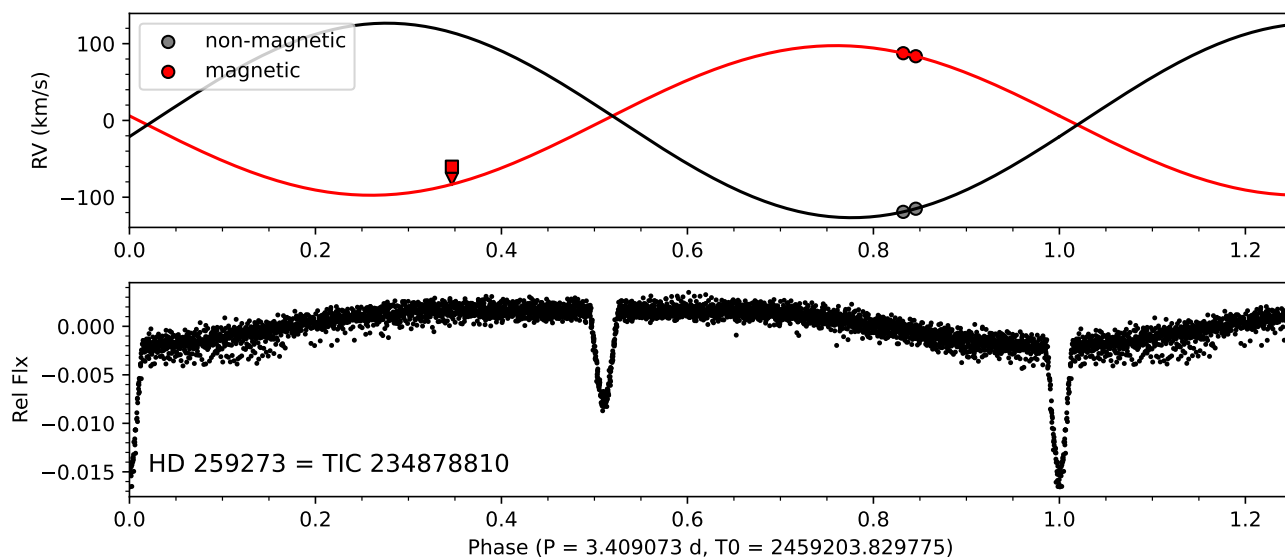


**Fig. B.3.** *TESS* light curve of HD 259273 (bottom) from sectors 6 and 33, phased to the orbital period, after removing the  $\sim 15.5$  day signal. The upper panel shows the RV measurements from the two ESPaDOnS Stokes I spectra taken for both components (red and black circles for the magnetic and non-magnetic stars respectively). The RV measurements from LAMOST are indicated by a red square (for the red arm of the spectrograph) and triangle (for the blue arm). A sinusoid is fit to the ESPaDOnS RVs to give a qualitative impression of the expected RV curves, but is not quantitatively reliable with just two closely-spaced measurements.